# 1
# Containerless Undercooling of Drops and Droplets

*Dieter M. Herlach*

## 1.1
## Introduction

Containerless processing of droplets has a long traditional experience. In his work *Discorsi e Dimostrazioni Matematiche intorno a due nuove scienze* published in 1639, Galileo Galilei describes experiments in which materials of different specific mass density were dropped down to ground from the leaning tower of Pisa to demonstrate that bodies of different mass fall with same velocity if friction in the air is neglected. In 1799, it was reported that a drop tower was used to produce lead shots by containerless solidification of liquid droplets during free fall. Liquid lead was pressed through a sieve at the top of the drop shaft to produce droplets of unique size, which solidified during free fall. The conditions of reduced gravity during free fall favored an ideal sphere-like geometry of the droplets upon solidification.

If a droplet is containerless solidified, often the liquid cools down below the equilibrium melting temperature prior to solidification. By using containerless processing methods, large undercoolings can be achieved since heterogeneous nucleation on container walls is completely avoided that is otherwise initiating crystallization of the melt. Nowadays, a great variety of techniques are applied for containerless undercooling. One distinguishes between drop tubes for containerless solidification of a spray of droplets, drop towers to process individual drops during free fall, and levitation techniques. Small drop tubes are quite suitable to study the statistics of phase and microstructure formation of particles on size less than 1 mm. The droplets are solidifying during free fall inside the drop tube. Thus, drop tubes are in house facilities to study solidification under reduced gravity conditions. For instance phase selection diagrams can be constructed such that they are describing the formation of competing phases in dependence of the droplet size, or the cooling rate since the droplet size directly correlates to the cooling rate [1]. Large drop tubes in height up to 150 m enable solidification of individual drops in size up to several millimeters. They are used to study the glass-forming ability of metallic alloys [2]. The temperature profile of drops falling under ultrahigh-vacuum conditions is recorded

*Solidification of Containerless Undercooled Melts*, First Edition. Edited by D.M. Herlach and D.M. Matson

by a set of photodiodes arranged along the dropt tube. In such a way phase selection of refractory alloy systems is studied as a function of undercooling [3].

Drop towers and drop shafts are differing from drop tubes in such that experiment facilities are falling and samples can be studied under reduced gravity conditions for a period of 4.5 s at a falling distance of 150 m (drop tower in Bremen) and 9 s at falling distance of 500 m (drop shaft in Hokkaido), respectively. In all drop tubes and drop towers, it is difficult if not at all impossible to perform *in situ* diagnostics of solidification of metallic drops.

Levitation techniques offer the great potential not only to containerless undercool and solidify drops in size up to 10 mm but they can also be combined with proper diagnostic means and allow for even stimulate solidification of freely suspended drops externally at various undercooling levels. A simple quasilevitation technique was frequently used to undercool a liquid metal or alloy by embedding it into a denucleation agent. In such a way, contact to the solid container is avoided, and in most cases the melt fluxing agent removes heterogeneous motes on the surface of the molten drop [4]. However, this technique is limited by the need to avoid chemical reactions between fluxing agent and liquid metal. Electromagnetic levitation was developed for containerless undercooling and solidification of metallic systems. The eddy currents induced by an alternating, inhomogeneous electromagnetic field create a secondary field that is opposite to the primary one. Thus, the eddy currents will create a repulsive force. If a properly designed coil is used and the coil current is adjusted, the repulsive force compensates the gravitational force and the sample is electromagnetically levitated. The eddy currents induced by alternating electromagnetic field cause at the same time heating the sample. Coupling of levitation and heating gives the advantage that no extra heating source is required, however, leads to the disadvantage that temperature control is only possible in a range at elevated temperature since levitations needs a minimum power absorption to guarantee a freely suspended drop [5]. This boundary condition is circumvented by applying electrostatic levitation. Here, a sample in diameter of 2–3 mm is electrically charged up and levitated in a strong electrostatic field. In most cases a laser is used to heat the sample [6]. Whereas the electromagnetic levitation is a self-stabilizing method, the electrostatic levitation needs a sophisticated sample positioning and a real-time electrostatic field control, since the sample is always in an unstable position (Earnshow theorem). Other methods like aerodynamic and acoustic levitation are frequently used for organic substances and oxides. They are not favorable techniques to undercool high melting metals. On the one side, a liquid metal changes at high temperatures the local levitation conditions, and more seriously, some residual amounts of oxygen in the environmental processing gas leads to the formation of metal oxides at the surface of the metallic drop. Sine metal oxides are in most cases thermodynamically more stable than the parent metal, they act as heterogeneous nucleation sites and limit the accessible undercooling range. Therefore, these techniques are not further dealt with in the present book.

The special environment of reduced gravity during parabolic flight and in Space offers the great advantage that the forces to compensate disturbing accelerations are by orders of magnitude smaller than the force needed to compensate the gravitational

force on Earth. Moreover, in case of electromagnetic processing the stirring of the melt due to the eddy currents are much reduced. The German Space Agency Deutsche Agentur für Raumfahrtangelegenheiten DARA, now Deutsches Zentrum für Luft- und Raumfahrt – Raumfahrtagentur (DLR Space Agency) – has developed an electromagnetic levitator for the use in reduced gravity. It applies a new technical concept such that two different frequency generators operating at different frequencies power a coil for positioning by a quadrupole field and, separately from that, a coil that produces a dipole field for efficient heating [7]. This concept was mandatory to develop a levitator for the usage in Space since it increased the efficiency in energy consumption of high-frequency generators for levitation from 1 to 2% (conventional high-frequency generators) to more than 30%. This device, called TEMPUS (German acronym for containerless processing in reduced gravity, *Tiegelfreies Electro-Magnetisches Prozessieren Unter Schwerelosigkeit*) was successfully tested in the realistic environment in Space by three NASA Spacelab missions, IML2 (1994), MSL1, and MSL1R (1997). At the same time very interesting results were obtained in measuring thermophysical properties of liquid metals and alloys even in the metastable regime of the undercooled melt, and in investigating phase selection and dendrite growth in reduced gravity [8]. Basing upon the success of TEMPUS, DLR, and ESA are currently developing in a common effort, an electro*m*agnetic levitator (EML) as a multiuser facility on board the *I*nternational *S*pace *S*tation (ISS). Thanks to the national agencies and the European Space Agency (ESA), several international researcher teams are preparing experiments using the EML on board the ISS. These experiments are divided into four different classes: (i) solidification, (ii) measurements of surface tension and viscosity, (iii) measurements of thermodynamic properties, and (iv) measurements of the mass density and thermal expansion. In the present book we concentrate on solidification comprising both experimental research in drop tubes and levitation devices on Earth and some specific experiments in Space. These experimental works are escorted by theoretical works as mesoscopic modeling of dendrite growth and atomistic modeling of attachment kinetics of atoms from liquid to solid.

In the present chapter, facilities for containerless solidification of undercooled melts are introduced. Their technical concepts are described and some exemplary results are demonstrated as obtained from experiments using the various devices.

## 1.2 Drop Tubes

The drop tube technique is employed to cool and solidify small molten droplets, which fall containerlessly down a tube that can be evacuated and backfilled with processing gases such as He, Ar, or others. It is convenient to distinguish between two categories of tubes – short and long – which reflect the type of the experiment that can be performed. In short drop tubes, a liquid jet of material is produced that disperses into many small droplets. In long drop tubes, individual drops in size of a few millimetres are undercooled and solidified during free fall.

### 1.2.1 Short Drop Tubes

Sample material in mass of several grams is melted in a crucible, which contains a small bore at its lower side. By using Ar gas at overpressure, the liquid metal is pressed through the bore of the crucible. A thin liquid jet of a metal is formed and it disperses into small droplets (Rayleigh instability of a thin liquid jet). The small droplets undercool and solidify during the free fall containerlessly in reduced gravity. This technique is employed to study undercooling and nucleation phenomena [9–11], to investigate the evolution of grain-refined microstructures [12, 13], and to produce metastable crystalline materials and metallic glasses [9–11, 14, 15].

Figure 1.1 illustrates the experimental setup of a drop tube in length of 14 m (free fall time 1.4 s) at the German Aerospace Center (DLR) in Cologne [16]. The drop tube is made of stainless steel components all of which are compatible with the requirements of ultrahigh vacuum (UHV) technique. The drop tube is evacuated before each experiment to a pressure of approximately $10^{-7}$ mbar and, subsequently, backfilled with high purity He or He–$H_2$ gas of high thermal conductivity. The processing gas is purified as it passes a chemical oxygen absorption system and a liquid nitrogen cold trap. The sample material in a crucible of, for example, fused silica, is melted inductively. After all the material is liquid, its temperature is measured by a two-color pyrometer and subsequently forced by Ar pressure of 2 bars through the small bore. The droplets solidified during free fall through the drop tube they are collected at the bottom of the drop tube and are sorted by meshes in different size groups ranging from 50 to 1000 μm diameter. Since the droplet diameter scales with the cooling rate at which the droplets cool down, drop tubes are quite suitable to study statistical processes of phase selection and their temperature–time–transformation behavior.

Figure 1.2 shows the volume fractions of the various phases formed in drop tube processed $Al_{88}Mn_{12}$ alloy as a function of droplet diameter [1]. Quasicrystalline phases of fivefold symmetry were discovered as a new class of solid-state matter in between of crystalline and amorphous solids in melt spun ribbons of $Al_{88}Mn_{12}$ alloy [18]. Depending on the preparation conditions, an icosahedral I-phase with quasiperiodicity in three dimensions, a decagonal T-phase with quasiperiodicity in two dimensions, and periodicity in the third dimension and different crystalline phases are solidified in this alloy. The drop tube experiments reveal that the I-phase is formed far from equilibrium in the smallest droplets at highest cooling rate. At medium droplet size, T-phase and supersaturated $Al_{ss}$ solid solution are found. The mass fraction of $Al_{ss}$ phase increases with droplet size (decreasing cooling rate) on the expense of T-phase. At largest droplet size of drops in the order of about 1 mm in diameter, also the equilibrium intermetallic phase $Al_6Mn$ is crystallized. Calculations of nucleation–kinetics plots reproduce the experimentally observed phase-selection behavior of drop tube processed $Al_{88}Mn_{12}$ alloy [19].

Drop tube experiments are also used to determine the formation of different phases selected kinetically by the cooling rate. Temperature–time–transformation (TTT)

curves are constructed such that they show the kinetics of phase formation of the various phases individually involved in solidification of undercooled melts in multicomponent multiphase alloys. To do so the Avrami analysis [20] is utilized that describes the time $t$ necessary to produce a mass fraction $X = 10^{-3}$, which is barely detectable by experimental diagnostics (X-ray diffraction, optical and electron microscopy), of the equivalent phases formed at a certain undercooling. It is given by

$$X = I_{ss} V^3 t^4 \tag{1.1}$$

with $I_{ss}$ the steady-state nucleation rate and $V$ the crystal growth rate. The crystal growth velocity in quasicrystal forming alloys is extremely sluggish. This is because it requires short-range diffusion of the various atomic species to arrange them in a correct way at the solid–liquid interface to form the complex structure of quasicrystalline phases [21]. The propagation of the solidification front into the undercooled melt is essentially driven by the kinetic undercooling of the interface. Under such circumstances, the speed of the solidification front is estimated by the rate theory leading to

$$V = \frac{D}{a_0}\left[1 - \exp\left(\frac{\Delta G_{LS}}{k_B T}\right)\right] \tag{1.2}$$

The TTT curves suggest an undercooling range of 150–200 K in drop tube processing. They predict a sequence of phase formation with the cooling rate as experiment parameter. At small cooling rates $Al_6Mn$ intermetallic and crystalline Al preferably solidify. At cooling rates exceeding 1000 K $s^{-1}$, the intermetallic $Al_6Mn$ phase disappears, while the quasicrystalline T-phase progressively forms. Further increasing the cooling rate to $1 \times 10^4$ K $s^{-1}$ leads to solidification of the quasicrystalline I-phase. In order to avoid the nucleation of quasicrystalline phases and in particular the crystalline Al-phase, very large cooling rates greater than $10^6$ K $s^{-1}$ are needed. This is in accordance with the observation that quasicrystalline phases nucleate quite easily in undercooled melts and the formation of amorphous phases in quasicrystal forming alloys during rapid cooling of a liquid is very difficult. Figure 1.3 summarizes the TTT diagrams for the various phases formed from the undercooled melt of $Al_{88}Mn_{12}$ alloy taking into account the experimental results of the drop tube experiments [19].

### 1.2.2
### Long Drop Tubes

Long drop tubes are generally in excess of 50 m high and individual drops are processed. They exploit the fact that a body falling freely in *vacuo* experiences zero gravity, to study the effects of microgravity on solidification in earthbound laboratories. There are two such facilities: a 105-m drop tube at NASA Marshall Space Flight Center, described by Rathz *et al.* [23], and a 47-m drop tube at the Nuclear Research

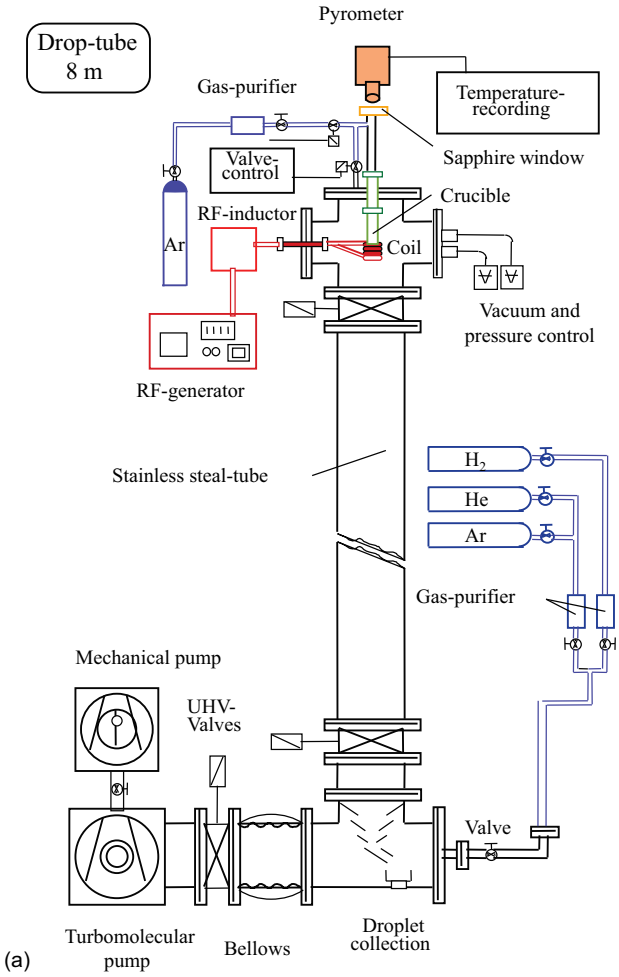
Drop-tube
8 m
Pyrometer
Gas-purifier
Temperature-
recording
Sapphire window
Valve-
control
Crucible
RF-inductor
Ar
Coil
Vacuum and
pressure control
RF-generator
Stainless steal-tube
H2
He
Ar
Gas-purifier
Mechanical pump
UHV-
Valves
Valve
Turbomolecular
pump
Bellows
Droplet
collection

(a)

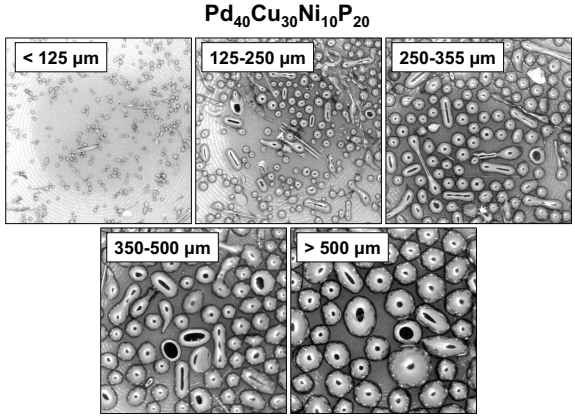
Pd40Cu30Ni10P20
< 125 µm
125-250 µm
250-355 µm
350-500 µm
> 500 µm

(b)

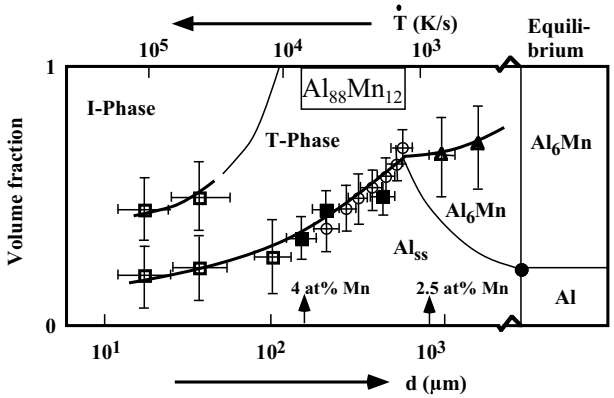


**Figure 1.2** Phase mixture in droplets of $Al_{88}Mn_{12}$ alloy as a function of droplet diameter. The large droplets crystallize a mixture of equilibrium $Al_6Mn$ phase and supersaturated solid solution $Al_{ss}$, while with decreasing droplet size (increasing cooling rate) quasicrystalline T- and I-phase are formed progressively [1].

Center at Grenoble [24]. In experiments using such facilities the tube is evacuated and single droplets 1–5 mm in diameter are melted by an electron beam (pendant drop technique) or electromagnetic levitation. After release, the droplet is monitored by Si or InSb photodiodes along the length of the tube, which enable the recalescence event to be detected. The time-of-flight before this event is measured and used with a heat flow model and the initial droplet temperature to estimate the undercooling achieved at nucleation $\Delta T_n$. Processing of drops under high vacuum [23] or even UHV [24] reduces surface oxidation of the molten samples as a possible source of heterogeneous nucleation. On the other hand only high melting metals as, for example, refractory metals can be processed since cooling is only by radiation, which is efficient at high temperatures exclusively. Lacy *et al.* found the mean undercooling in niobium to be $525 \pm 8$ K with a maximum of 535 K [25]. They associated this nucleation event with the formation of NbO on the droplet surface because the nucleation temperature corresponded to the melting temperature of this oxide. These results show that high vacuum conditions are not sufficient to avoid heterogeneous nucleation due to surface oxidation, but UHV may lead to an improvement. In fact, the highest absolute undercooling was measured on droplets processed in the Grenoble drop tube. Vinet *et al.* report a maximum undercooling of 900 K for Re [3].

**Figure 1.1** (a) Schematic view of the DLR drop tube; the drop tube technique combines rapid cooling of small particles and reduction of heterogeneous nucleation by containerless processing and by dispersion of the melt into a spray of small droplets; (b) droplets of $Pd_{40}Cu_{10}Ni_{30}P_{20}$ alloy as solidified in the drop tube and sorted in different size groups [17]. The drops do not show all sphere-like geometry since the alloy is an easy glass forming system that is characterized by a high viscosity. This leads to cylindrical shape of the fragmented portion of the liquid metal that undercools and solidifies at large undercoolings at which the viscosity of the melt has essentially increased.

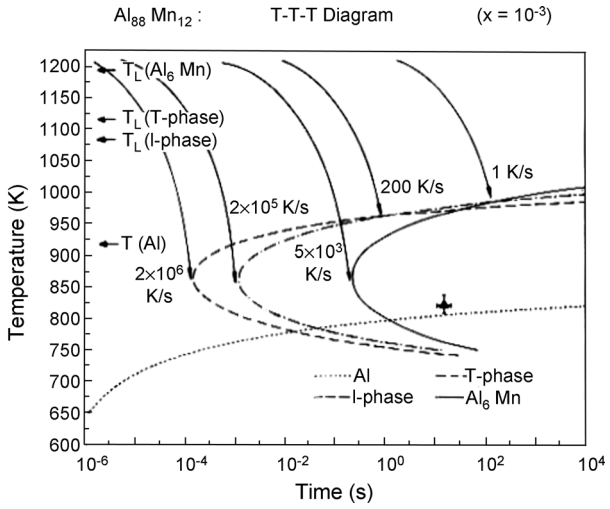


**Figure 1.3** Temperature–time–transformation diagrams of the various phases involved in the solidification of undercooled droplets of $Al_{88}Mn_{12}$ assuming a fixed volume fraction of $X = 10^{-3}$ [19]. Critical cooling rates are also shown for the avoidance of crystallization of various phases. The solid triangle corresponds to the maximum undercoolability of the Al-phase in Al–Mn alloys as investigated by the droplet-dispersion technique [22].

The high value of undercooling together with the observation of polycrystalline microstructure in the as-solidified sample was taken to assume homogeneous nucleation to be present in this experiment. They used the undercooling result to estimate the solid–liquid interfacial energy by an analysis within homogeneous nucleation theory.

Drop tube experiments are complementary to levitation experiments. In both techniques, the samples are processed containerlessly. While levitation experiments allow measuring the whole history of undercooling and solidification, drop tubes offer the possibility of statistical analysis of nucleation and crystal growth as a function of droplet size and cooling rate.

## 1.3 Containerless Processing Through Levitation

A freely suspended drop without any contact to a solid or liquid medium is generated by employing levitation techniques. Levitation of bulk samples offers the unique possibility of undercooling bulk samples, which remain accessible not only for direct observation but also for external stimulation of nucleation. The current state of electromagnetic and electrostatic levitation is described.

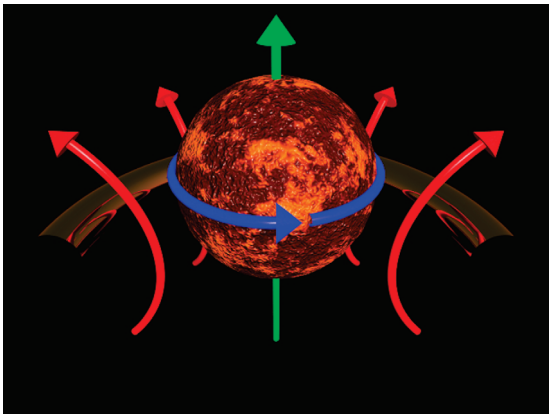

**Figure 1.4** Schematics of electromagnetic levitation; the red arrows indicate the magnetic field of the levitation coil. The blue arrows represent the eddy currents induced within the sample by the alternating electromagnetic field. The eddy currents, in turn, produce a magnetic field that is opposite to the primary magnetic field due to a phase shift by $\pi$ between the electrical current in the coil and the induced eddy currents. This leads to a repulsive force indicated by the green arrow. At properly designed coil geometry and coil current, the repulsive force compensates the gravitational force [27].

### 1.3.1 Electromagnetic Levitation

For metallic systems the most suitable technique for freely suspending spheres of diameter up to 1 cm is the electromagnetic levitation technique. The schematic of electromagnetic levitation is illustrated in Figure 1.4. The principle of electromagnetic levitation is based on the induction of eddy currents in an electrically conducting material if the material experiences a time-dependent magnetic field $B$ (Lenz rule)

$$\nabla \times E = -\partial B/\partial t \tag{1.3}$$

with $E$ the electrostatic field. For a nonuniform magnetic field, the eddy currents induced in a sample produce a magnetic dipole moment $m$ that is opposite to the primary field $B$. This leads to a diamagnetic repulsion force $F_r$

$$F_r = -\nabla(m \cdot B) \tag{1.4}$$

between the primary field und the sample. If the repulsion force $F_r$ is equal in amount and opposite in direction to the gravitational force, $F_r = m_g g$, the sample is levitated. $m_g$ denotes the mass of the sample and $g$ the gravitational acceleration. Electromagnetic levitation can be used to levitate metallic and even semiconducting samples. However, electromagnetic levitation of semiconductors requires either doping with a metallic element to increase the electrical conductivity or preheating the pure semiconductor to a temperature of about 1000 K by a laser or by a graphite susceptor within the levitation coil so that the intrinsic conduction is sufficiently increased to

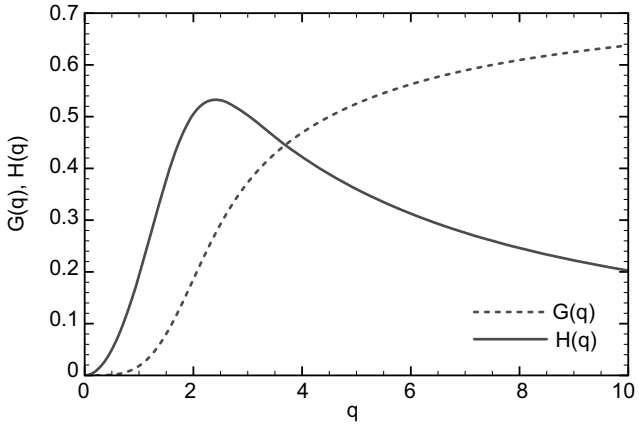


**Figure 1.5** Efficiency of the function $G(q)$ (dashed line) which is proportional to the levitation force $F_{em}$, and the function $H(q)$ (solid line) which is proportional to the power absorption $P$ [27].

electronically couple the sample to the alternating external field. A characteristic feature of electromagnetic levitation is that both levitation and heating of the sample are always occurring simultaneously. This offers the advantage that no extra source of heating is required to melt the material, but it is associated with the disadvantage that levitation and heating can be controlled independently only in a very limited range.

According to Rony [26], the mean force on an electrically conductive nonferromagnetic sample is determined by

$$F_{\mathrm{em}} = -\frac{4\pi r}{3} \cdot \frac{B \cdot \nabla B}{2\mu_o} \cdot G(q) \tag{1.5}$$

Here, $r$ denotes the radius of the sphere-like sample, $\mu_o$ the permeability of vacuum. The function $G(q)$ is calculated as

$$G(q) = \frac{3}{4}\left(1 - \frac{3\sinh(2q) - \sin(2q)}{2q\cosh(2q) - \cos(2q)}\right) \tag{1.6}$$

$q$ is the ratio of the sample radius and the skin depth

$$q = \frac{r}{\delta} \quad \text{with} \quad \delta = \sqrt{\frac{2}{\mu\omega\sigma}} \tag{1.7}$$

$\omega$, $\sigma$, and $\mu$ are the angular frequency of the electrical current, the electrical conductivity, and the magnetic permeability of the sample, respectively. According to Eq. (1.5) the levitation force scales with the gradient of the magnetic field. To optimize levitation, it is therefore crucial to design properly the geometry of the levitation coil and optimize the function $G(q)$. This function is plotted versus $q$ in Figure 1.5 (dashed line). Consequently, the efficiency of electromagnetic levitation is adjusted by the parameters of the frequency of the alternating electromagnetic field, the sample size, and the electrical conductivity of the sample. For a vanishing

conductivity ($q \rightarrow 0$), $G(q)$ becomes zero and levitation is not possible. For $G(q \rightarrow \infty)$ $G(q)$ is approaching saturation.

To levitate a sample of masse $m$, the gravitational force $F_g$ has to be compensated by the electromagnetic levitation force $F_{\mathrm{em}}$

$$F_{\mathrm{em}} = -F_g, \quad F_g = m \cdot g = \frac{4\pi r^3}{3} \varrho \cdot g \tag{1.8}$$

where $\varrho$ denotes the mass density of the material. The $z$-component of the force follows as

$$\frac{\partial B^2}{\partial z} = \frac{2\mu_o g}{G(q)} \cdot \varrho \tag{1.9}$$

For a given magnetic field and sample size, the levitation force is determined by the skin depth $d$ and the mass density $m$. The mean power absorption $P$ is calculated according to Roney as

$$P = \frac{B^2}{2\mu_o} \cdot \omega \cdot \frac{4\pi r^3}{3} \cdot H(q) \tag{1.10}$$

with

$$H(q) = \frac{9}{4q^2} \cdot \left( q \cdot \frac{\sin \mathrm{h}\,(2q) - \sin\,(2q)}{\cos \mathrm{h}\,(2q) - \cos\,(2q)} - 1 \right) \tag{1.11}$$

$H(q)$ is the efficiency of the power absorption as illustrated by the solid line in Figure 1.5. For vanishing electrical conductivity no power is absorbed by the sample. On the other hand for an ideal conductor no ohmic losses occur so that $H(q)$ converges to zero. The function $H(q)$ passes through a maximum at $q \approx 2$.

The concept developed by Rony has been extended and applied by Fromm and Jehn to calculate both the levitation force and the power absorption for a levitation coil that is approximated by different single loops being parallel to each other [28, 29].

The temperature control of electromagnetically levitated samples requires a separate action of $P$ and $F_{\mathrm{em}}$ as far as possible. The essential difference between $P$ and $F_{\mathrm{L}}$ is that the functions $G(q)$ and $H(q)$ have a different characteristics with respect to the frequency of the alternating electromagnetic field: $F_{\mathrm{em}}$ depends on the product $(B \cdot \nabla)B$, while $P$ is proportional to $B^2$ (cf. Eqs. (1.5) and (1.10)). Hence, temperature control is possible within a limited range by choosing a proper frequency of the alternating field and by a movement of the sample along the symmetry axis of a conically shaped coil. In the lower regions of the coil, the windings are tighter, and thus the magnetic field and power absorption are greater than that in the upper region of the coil with lower field strength. By increasing the power, the sample is lifted up into regions of larger field gradients and smaller magnetic field strength and cools down.

Using coils of suitable geometry, controlled temperature variation is possible by several 100 K. By changing the sample position in the levitation coil due to a variation of the current through the coil, the temperature of a Ni sample ($\varnothing \approx 8$ mm) may be

altered within a range of approximately 600 K. It is assumed that the sample is placed into a levitation coil with six windings and two counter-winding at its top. An alternating electrical current at 300 kHz powers the coil. More details on this analysis of temperature control may be taken from reference [30].

Under equilibrium conditions, the sample approaches a temperature that is given by the balance of heat produced in the sample and loss of the heat of the sample to the environment. For a containerlessly processed droplet, the loss of heat is possible by heat radiation, $\dot{Q}_{\mathrm{rad}}$, and – if an environmental gas atmosphere is present – by heat conduction and convection, $\dot{Q}_{\mathrm{con}}$, in the environmental gas. Thus, the balance is given by

$$P = \dot{Q}_{\mathrm{rad}} + \dot{Q}_{\mathrm{con}} \tag{1.12}$$

According to Planck's law, the heat transfer by radiation is given by

$$\dot{Q}_{\mathrm{rad}} = \sigma_{\mathrm{SB}} \varepsilon A \cdot (T^4 - T_{\mathrm{o}}^4) \tag{1.13}$$

where $\sigma_{\mathrm{SB}} = \dfrac{2\pi^3 k_{\mathrm{B}}}{15 h^3 c^2} \approx 5.67 \times 10^{-8}$ $\mathrm{Wm^{-2}K^{-4}}$ denotes the Stefan–Boltzmann constant, $\varepsilon$ the total emissivity of the sample, $A$ the surface area of the sample, $T$ the temperature of the sample, and $T_{\mathrm{o}}$ the ambient temperature. Since the Stefan–Boltzmann constant is very small, heat transfer by radiation becomes important only at elevated temperatures of $T > 1000$ K, but increasing then rapidly because of the fourth power of the $T$ dependence. This means that in most cases radiation cooling is not sufficient to cool and undercool a metallic sample below its melting temperature. Therefore, cooling by an environmental gas is employed. The heat transfer by conduction can be approximated by

$$\dot{Q}_{\mathrm{con}} = A \cdot \lambda_{\mathrm{eff}} (T - T_o) \tag{1.14}$$

where $\lambda_{\mathrm{eff}}$ is an effective heat transfer coefficient including both heat conduction and heat transport by convection in the surrounding gas atmosphere.

A schematic view of an electromagnetic levitation chamber for containerless undercooling and solidification experiments is shown in Figure 1.7 [32]. The levitation coil together with the sample (Ø ≈ 6 mm) is placed within an ultra-high-vacuum chamber, which can be backfilled with gases such as He or He–$H_2$ mixture. The gases are purified by an oxygen absorption system and, additionally, by passing them through a liquid nitrogen cold trap. The sample is processed within the levitation coil, which is powered by a high-frequency generator. The maximum power output of the radio-frequency generator is 24 kW. The frequency can be changed in the range between 300 kHz and 1.2 MHz. Temperature control in a limited range is possible by using forced convection with cooling gases. The temperature of the sample is measured by means of a two-color pyrometer with an absolute accuracy of ±3 K and a sampling rate up to 1 kHz. Solidification of the undercooled melt can be externally initiated by touching the sample with a crystallization trigger needle.

Figure 1.8 depicts a typical temperature–time profile recorded contactless by a pyrometer during an undercooling experiment of an alloy. During heating the sample

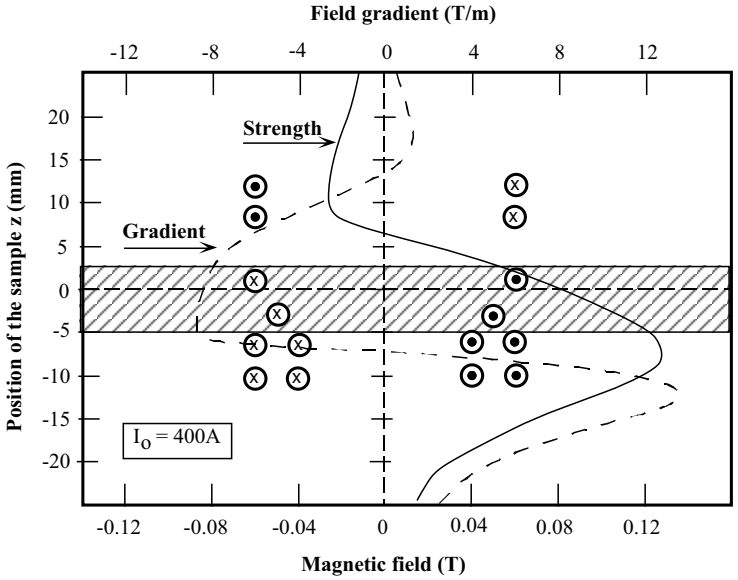


**Figure 1.6** Strength (solid line) and gradient (dashed line) of the magnetic field as a function of the sample position of a typical levitation coil developed for undercooling experiments on gold [31]. The dashed area gives the range of positions in which the sample can stably be levitated. A coil current of $I_o = 400$ A has been assumed.

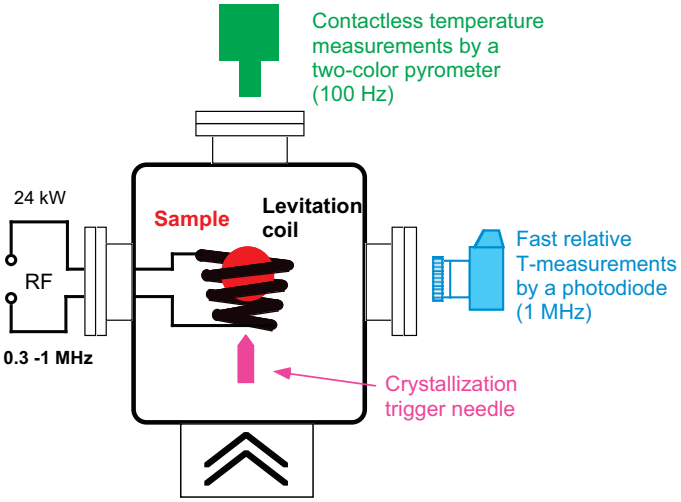


**Figure 1.7** Electromagnetic levitation chamber for containerless undercooling and solidification of metals.

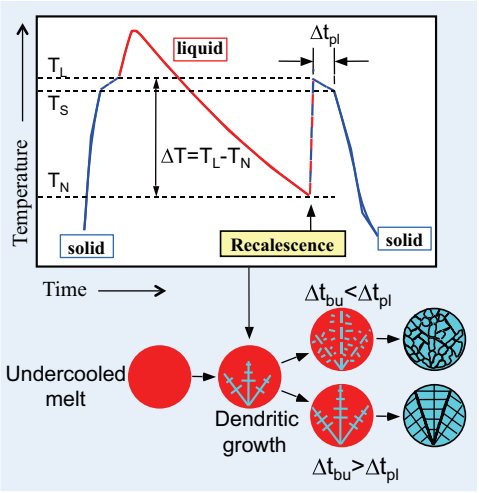


**Figure 1.8** Schematics of a typical temperature–time ($T$–$t$) profile obtained from an undercooling experiment using electromagnetic levitation. The undercooling $\Delta T$ and the plateau duration $\Delta t_{pl}$ are directly inferred from experimental profiles. If the time needed to break up a dendrite, $\Delta t_{bu}$ is smaller than the postrecalescence or plateau time, $\Delta t_{pl}$ dendrites will break up leading to a grain-refined equiaxed microstructure. In the other case, the undercooled melt will crystallize to a coarse-grained dendritic microstructure.

melts in the interval between $T_L$ (liquidus temperature) and $T_S$ (solidus temperature) marked by a change in the slope of the temperature–time trace. After heating the sample to a temperature well above the liquidus temperature, the sample is cooled and undercooled to a temperature $T_N$ at which nucleation is externally triggered. Crystallization then sets in, leading to a rapid temperature rise during recalescence due to the rapid release of the heat of crystallization. During recalscence, solidification takes place far away from equilibrium and the undercooled melt acts as a heat sink. Dendrites form at the nucleation point and propagate rapidly through the volume of the melt. Once the temperature has reached a value between $T_L$ and $T_S$, the remaining interdendritic melt solidifies during a "plateau phase" under near-equilibrium conditions. The plateau duration $\Delta t_{pl}$ is exclusively controlled by the heat transfer from the sample to the environment and is inferred from the measured temperature–time profile. $\Delta t_{pl}$ is essentially an experimental control parameter, which can be varied by changing the cooling rate. After all the liquid is solidified, the sample cools down to ambient temperature. By exceeding a critical undercooling, the solidification mode changes from coarse-grained dendriditic to grain-refined equiaxed microstructure. The refinement of the microstructure is caused by remelting and coarsening of primarily formed dendrites. The transitional microstructures indicate the presence of sphere-like particles in the wake of a dendritic microstructure. This suggests that the sphere-like elements originate from the break-up of primary dendrites and their side-branches by remelting. Physically, this process is driven by surface tension: the system attempts to minimize its solid–liquid interface

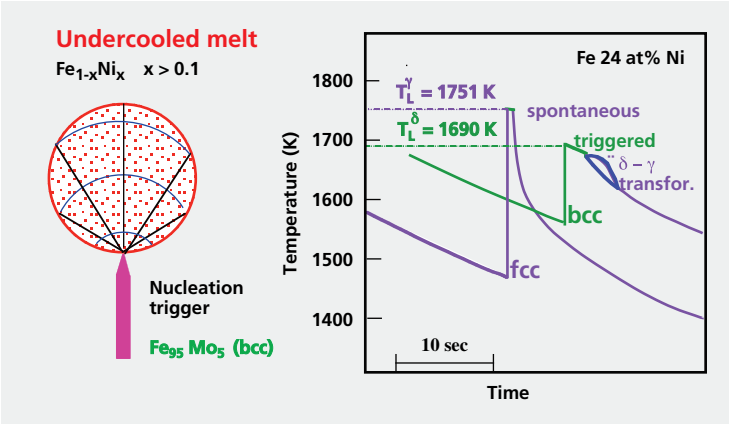


**Figure 1.9** (a) Principle of nucleation triggering of a metastable bcc phase in $Fe_{76}Ni_{24}$ alloy by using a nucleation trigger made of $Fe_{95}Mo_5$ bcc phase (b). Two temperature–time profiles obtained during solidification of undercooled $Fe_{76}Ni_{24}$ alloy. Spontaneous crystallization of stable fcc phase (γ, blue line), and solidification of a metastable bcc phase upon triggering with the $Fe_{95}Mo_5$ nucleation trigger (green line).

area via heat and solute diffusion in the bulk phases. The fragmentation process itself requires atomic diffusion in liquid phase. During the postrecalescence time, primary solidified dendrites coexist with interdendritic liquid. Therefore, the condition for dendrite break up is given if the dendrite break up time is smaller than the postrecalescence time. In the other case, the primary solidified dendrites survive leading to coarse-grained dendritic microstructures. The postrecalescence time is inferred from the measured temperature–time profiles while the dendrite break up time is calculated within a fragmentation model developed by Karma [33]. This model is verified by experiments on levitation-undercooled samples in which the microstructures are investigated as a function of undercooling prior to solidification. More details about the dendrite fragmentation process are given in [34].

The crystallization needle is used to trigger externally solidification at preselected undercooling and well-defined position at the surface of the sample. In such a way the crystallization kinetics is investigated as a function of undercooling [35]. Figure 1.9 illustrates triggered nucleation of a metastable bcc phase of Fe-24at%Ni alloy. A trigger needle made of a $Fe_{95}Mo_5$ alloy is used since this alloy forms a stable bcc structure in the temperature range of the present experiment. The left peak represents a recalescence event as observed following spontaneous nucleation at 1472 K ($\Delta T = 278$ K). An increase in temperature up to 1751 K during recalescence is found in good agreement with the equilibrium liquidus temperature of this alloy. The right peak was observed following solidification triggering with the Fe–Mo tip at a temperature of 1556 K ($\Delta T = 194$ K). Obviously, the increase in temperature during recalescence ends at a temperature well below the equilibrium liquidus line, which points to a metastable bcc solidification product. Immediately following the recalescence peak, a weak hump is found in the cooling trace, which is due to a solid-state

transformation of metastable bcc phase into stable fcc phase. This hump is missing in the temperature–time profile for the spontaneous nucleation. This confirms that during spontaneous crystallization fcc phase is nucleated, whereas triggered solidification leads to nucleation of metastable bcc phase, which however transforms into stable fcc phase during cooling of the sample to ambient temperature [36].

The cooling rates in the order of 10–100 K $s^{-1}$ in the above-described undercooling experiments on Fe–Ni alloys are not sufficient to conserve the primary solidified metastable bcc phase during cooling to ambient temperatures. If the cooling rate is increased up to $10^5$–$10^6$ K $s^{-1}$ the solid-state transformation of primary formed bcc phase into the stable fcc phase can be, however, avoided. This has been demonstrated in the early drop tube experiments by Cech [37] and Cech and Turnbull [38], and later on by atomization experiments [39, 40]. Meanwhile, an electromagnetic levitation chamber is used to combine it with external diagnostic means, for example, neutron scattering and X-ray scattering by synchrotron radiation [41]. In such a way, the primary crystallization of a metastable bcc phase in Ni–V alloys at large undercoolings was directly evidenced by *in situ* energy dispersive X-ray diffraction on levitation-processed undercooled melt using high-intensity synchrotron radiation at the European Synchrotron Radiation Facility [42].

Electromagnetic levitation is also frequently applied to measure the dendrite growth velocity as a function of undercooling. This will be the subject of a separate Chapter 11.

### 1.3.2
### Electrostatic Levitation

Electromagnetic levitation requires sample material that is electrically conductive. Therefore, the application of electromagnetic levitation is restricted to metals and (doped) semiconductors. The advantage of electrostatic levitation is that levitation and heating is decoupled and the samples can be processed under conditions provided the vapor pressure of the processed material is small. However, there is a problem with the stability of the sample position. According to the theorem of Samuel Earnshow, it is not possible to levitate a charged sphere within a static electrostatic field [43].

Electrostatic levitation is based on the Coulomb forces acting on an electrically charged sample in a quasistatic electrical field [44]. A sample with a surface charge $q$ and a mass $m$ is levitated against gravity within a static electrostatic field $\vec{E}$ as

$$\vec{E} = -\frac{mg}{q} \cdot \vec{e}_z \tag{1.15}$$

$\vec{e}_z$ is the unit vector in the $z$ direction, that is, parallel to the electrostatic field. A stable position of the sample is based on a local potential minimum at $\vec{r}_o$ for all directions in space.

$$\frac{\partial^2}{\partial x^2}\Phi(\vec{r}_o) + \frac{\partial^2}{\partial y^2}\Phi(\vec{r}_o) + \frac{\partial^2}{\partial z^2}\Phi(\vec{r}_o) = \Delta\Phi(\vec{r}_o) > 0 \tag{1.16}$$

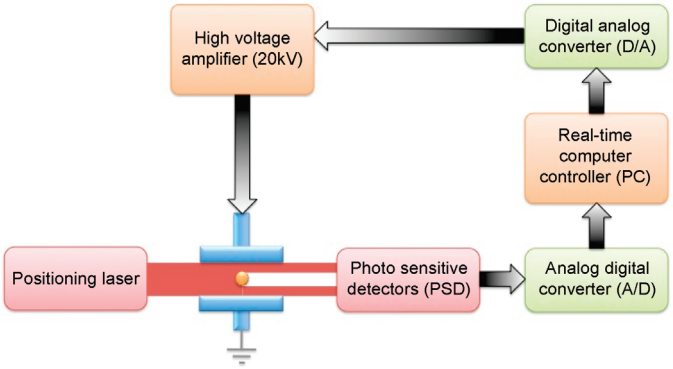


**Figure 1.10** Sketch of the fully automated active sample positioning system [45].

The Maxwell equation for Gauss's law affords

$$\Delta\Phi = -\frac{\varrho}{\varepsilon_o} \tag{1.17}$$

Under vacuum conditions, $\Delta\Phi = 0$. Hence, a potential minimum does not exist and a stable sample position under stationary conditions is not possible [27]. This means electrostatic levitation requires a sophisticated dynamic sample position and electrostatic field control. This became possible just since the 1990s of last century where high-voltage amplifiers were developed, which can be controlled with high slew rates of changing the voltage $U$, $\mathrm{d}U/\mathrm{d}t > 400\,\mathrm{V}\,\mu\mathrm{s}^{-1}$.

Figure 1.10 shows schematically the active sample positioning system. An electrically charged sample is levitated between two horizontal electrodes within a widened positioning laser beam filling the whole space between the electrodes. The sample shadow is detected by a two-dimensional photo-sensitive detector that gives information on the vertical and horizontal position of the sample. A real-time computer control algorithm developed by Meister [45] reads this information and adjusts instantaneously the voltage of the amplifier. In order to control the sample position in all three-dimensional directions, two positioning laser perpendicular to each other and an assembly of six electrodes are used. The arrangement of the electrodes is illustrated in Figure 1.11.

Two central electrodes arranged as a plate capacitor are surrounded by four electrodes in plane, which are cross-linked with the positioning lasers to push the sample in the central position. The forces acting in the $z$-direction, $F(z)$, are the gravitational force, the force due to the electrical field, and the force between the sample and the grounded center electrodes. With the method of image charges, the force of a charged sphere between the electrodes can be determined by

$$F(z) = \frac{q^2}{4\pi\varepsilon_o}\left(\sum_{n=1}^{\infty}\frac{1}{(2d_z n - 2z)^2} - \sum_{n=0}^{\infty}\frac{1}{(2d_z n - 2z)^2}\right) \tag{1.18}$$

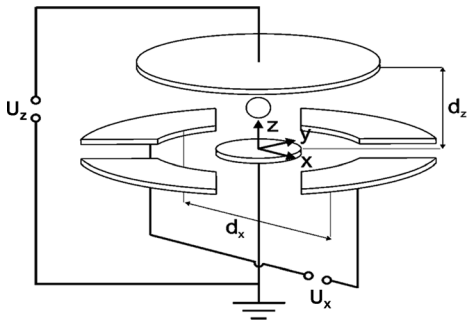


**Figure 1.11** Arrangement of the electrodes of the electrostatic levitator. The distances and connections of the *y*-direction are analogues and not printed for a better visualization.

with the position of the sample $z$, the distance of the electrodes $d_z$, the charge $q$ of the sample, the vacuum permittivity $\varepsilon_o$, and the number of reflections $n$. Neglecting multiple reflections, $F(z)$ is approximated as

$$F(z) \approx -\frac{q}{4\pi\varepsilon_o}\left(\frac{1}{(2z)^2}-\frac{1}{(2d_z-2z)^2}\right) \tag{1.19}$$

In the middle of the electrodes, the forces of the image charge acting on the sample are compensating each other. The equation of motion for the $z$ direction is given by

$$m\ddot{z} = -mg-q\frac{U_z}{d_z}-\frac{q^2}{4\pi\varepsilon_o}\left(\frac{1}{(2z)^2}-\frac{1}{(2d_z-2z)^2}\right) \tag{1.20}$$

The fields in the $x$- and $y$-direction are assumed to be between two parallel electrodes [45]

$$m\ddot{x} = -2q\frac{1}{\kappa}\cdot\frac{U_x}{d_x} \quad \text{with} \quad \kappa = \sqrt{\left(\frac{2z}{d_x}\right)^2+1} \tag{1.21}$$

$\kappa$ is a geometrical factor regarding the distance of the sample and the lateral electrodes.

For conducting an experiment using the electrostatic levitator, the sample in diameter of about 2–4 mm is placed at the lower electrode, which is grounded. The high-voltage power supply is switched on and electrostatic field between upper and lower electrode in the $z$-direction is built up. At the same time the sample is charged. Since the upper electrode is on negative potential, the surface of the sample is loaded with positive charge $q^i$ that is calculated as [46]

$$q^i = 4\pi\varepsilon_o L\frac{U_z}{d_z}r^2 \tag{1.22}$$

with $r$ the radius of the sample and $L = 1.645$ a geometrical factor. The image charge of the bottom electrode dominates the initial levitation voltage. The force acting on a sample while lifting is given by

$$F_z^i = \frac{4}{3}\pi r^3 \varrho g - q\frac{U_z^i}{d_z} - \frac{q^2}{4\pi\varepsilon_o}\cdot\frac{1}{(2r)^2} = 0 \tag{1.23}$$

Combining Eqs. (1.22) and (1.23) yields the initial voltage for levitation

$$U_z^i = \pm d_z\sqrt{\frac{4\varrho g r}{3L(4-L)\varepsilon_o}} \tag{1.24}$$

The charge of the sample in the beginning of the experiment is then

$$q^i = \mp 8\pi\sqrt{\frac{L\varepsilon\varrho g r^3}{3(4-L)}} \tag{1.25}$$

The voltage $U_z^o$ needed to keep the sample in the middle of the electrodes is calculated

$$U_z^o = \frac{4-L}{4}U_z^i \tag{1.26}$$

The initial voltage is larger than the voltage that is needed to levitate the sample in the middle of the horizontal electrodes. For a constant initial voltage, the time is approximated which elapses until the sample hits the electrode. This time is used to estimate the minimum sampling rate required for positioning. For a silicon sample in diameter of 2 mm the sampling rate is $2 \times 10^{-3}$ s [45].

Electrostatic levitation offers the advantage that positioning and heating are decoupled in contrast to electromagnetic levitation. Heating is realized in electrostatic levitation by an infrared laser. Increasing the temperature of the sample leads to an evaporation of surface atoms, which is useful for undercooling experiments since the evaporation cleans the surface and thereby reduces or even eliminates heterogeneous nucleation motes at the surface of the sample. On the other hand, the sample surface looses surface charge by evaporation. Therefore, the voltage has to be increased to keep the sample levitated. To facilitate recharging of the sample during levitation a focused ultraviolet light source with a high energy of several electronvolts ($\lambda = 115$–$350$ nm) is used. In addition to this procedure, the sample is also recharged at elevated temperatures by thermionic emission of electrons. More details about the electrostatic levitator build up and operated at DLR can be found in [27, 45, 47].

The electrostatic levitator is very suitable to study nucleation undercooling with special emphasis to homogeneous nucleation. To observe homogeneous nucleation, very large undercoolings have to be realized, since the onset of homogeneous nucleation gives the physical limit for maximum undercoolability of a melt. To realize such conditions, heterogeneous nucleation has to be eliminated. Electrostatic levitation under ultra-high-vacuum conditions is ideally suited for such experimental

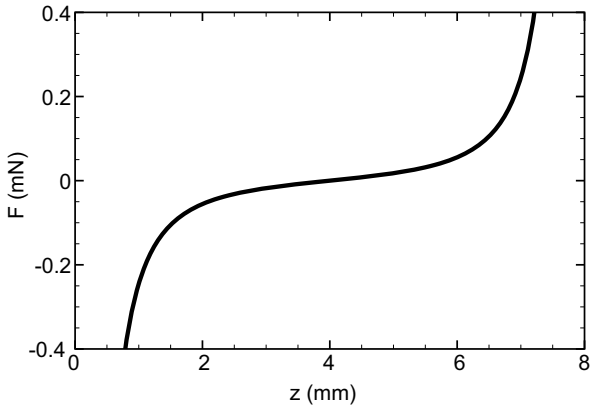


**Figure 1.12** Force on a charged sample for a distance of the plates of 8 mm generated by the image charges for an applied voltage. In the middle of the electrodes, the forces of the image charges are compensating each other.

studies since heterogeneous nucleation on container walls is completely avoided and heterogeneous nucleation on surface motes is reduced or even eliminated due to self-cleaning of the surface by evaporation at elevated temperature.

In the following, nucleation undercooling studies on pure Zr are presented to demonstrate that how physically different nucleation processes are experimentally investigated. Figure 1.13 shows a temperature–time profile measured on pure Zr

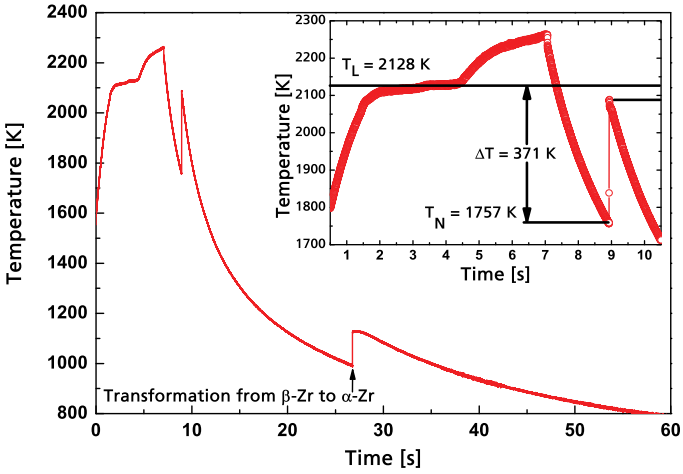


**Figure 1.13** Temperature–time profile measured on a zirconium drop levitated in an electrostatic levitator. The sample melts at $T_L = 2128$ K. During undercooling nucleation sets in at $T_N = 1757$ K. Subsequently, rapid crystal growth of β-Zr solid phase (bcc) leads to a steep rise of temperature during recalescence. The second recalescence event at 980 K is attributed to a transformation of solid β-Zr to solid α-Zr phase (hcp). The inset shows an enlargement of the recalescence profile with the nucleation temperature $T_N = 1757$ K and the undercooling $\Delta T = 371$ K.

sample in the electrostatic levitator. First, the solid sample is heated up to its melting temperature, $T_L$. In case of a pure metal as Zr, the sample melts congruently at $T_L$. The small step in the melting plateau is due to the change in spectral emissivity when the solid transforms to the liquid. After complete melting, the liquid sample is heated to a temperature well above $T_L$ before cooling. During subsequent cooling, the liquid sample undercools well below $T_L$. When spontaneous nucleation sets in at an undercooling $\Delta T = T_L - T_n$ ($T_n$: nucleation temperature) the nucleated crystal rapidly grows due to a large thermodynamic driving force generated at such deep undercoolings. The rapid release of the heat of crystallization leads to a steep rise in temperature during recalescence. From such temperature–time profiles, $\Delta T$ is easily inferred since $T_n$ is well defined by the onset of recalescence. After the entire sample has solidified, the next heating and cooling cycle is started.

Usually, the solidification of an undercooled metallic melt is a two-staged process. During recalescence, a fraction of the sample, $f_R$, solidifies during recalescence under nonequilibrium condition. The remaining melt, $f_{pr} = 1 - f_R$, solidifies under near-equilibrium conditions during postrecalescence period. $f_R$ increases with the degree of undercooling and becomes unity, $f_R = 1$ if $\Delta T = \Delta T_{hyp}$. The hypercooling limit, $\Delta T_{hyp}$, is reached if the heat of fusion $\Delta H_f$ is just sufficient to heat the sample with its specific heat $C_p$ up to $T_L$. In case of quasiadiabatic conditions, that is, if the amount of heat transferred to the environment is negligible compared to the heat produced during recalescence, the hypercooling limit is given by $\Delta T_{hyp} = \Delta H_f / C_p$. In case of pure Zr, the hypercooling limit is estimated as $\Delta T_{hyp} = 359$ K with $\Delta H_f = 14\,652$ J mol$^{-1}$ and $C_p = 40.8$ J mol K$^{-1}$ [6]. With increasing undercooling, $\Delta T' > \Delta T_{hyp}$, the postrecalescence plateau vanishes and $T_L$ will not be reached during recalescence. As can be seen from Figure 1.13, in this experiment an undercooling of $\Delta T = 371$ K is measured, which is larger than $\Delta T_{hyp}$.

Figure 1.14 shows the distribution functions of undercoolings measured in the electromagnetic levitator (Figure 1.14 left) and the electrostatic levitator (Figure 1.14 right). The experimental results are analyzed within a statistical model developed by Skripov [48]. According to nucleation theory [49], the activation energy $\Delta G^*$ for the formation of a nucleus of critical size is given by

$$\Delta G^* = \frac{16\,\pi}{3} \cdot \frac{\sigma^3}{\Delta G_V^2} \cdot f(\vartheta) \tag{1.27}$$

with $\sigma$ the solid–liquid interfacial energy, $\Delta G_V = G_L - G_S$ the difference of Gibbs free energy per unit volume of liquid, $G_L$ and solid $G_S$ phase, and $f(\vartheta)$ the catalytic potency factor for heterogeneous nucleation. In case of homogeneous nucleation, $f(\vartheta) = 1$. For pure metals, the driving force for nucleation, $\Delta G_V$, is approximated by $\Delta G_V = \Delta S_f \cdot T \cdot V_m^{-1}$ with $\Delta S_f = \Delta H_f / T_m$ and $\Delta H_f$ the enthalpy of fusion and $V_m$ the molar volume [50]. The solid–liquid interfacial energy $\sigma$ is given by the negentropic model [51] as

$$\sigma = \alpha \cdot \frac{\Delta S_f \cdot T}{\left(N_A V_m^2\right)^{1/3}} \tag{1.28}$$

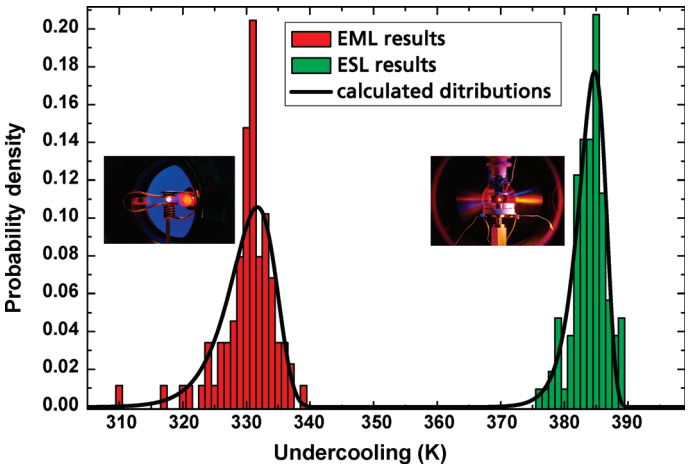


**Figure 1.14** Probability distribution functions of undercoolings measured in approximately 100 cycles on pure Zr in the electromagnetic (red bars) and the electrostatic levitator (green bars) [56]. The solid lines give the functions as computed according to a statistical analysis of nucleation within the Skripov model.

with $N_A$ Avogadro's number and $\alpha = 0.7$ for bcc structured solid β-Zr that primarily nucleates in the undercooled melt. The steady-state nucleation rate, $I_{ss}$, is computed by

$$I_{ss} = K_V \cdot \exp\left(-\frac{\Delta G^*}{k_B T}\right) = K_V \cdot \exp\left(-\frac{CT^2}{\Delta T^2}\right)$$
$$\text{with} \qquad (1.29)$$
$$K_V = \frac{k_B T N_o}{3 a_o \eta(T)}; \quad C = \frac{16\pi \Delta S_f \alpha^3 f(\vartheta)}{3 k_B N_A}$$

where $\eta(T)$ denotes the temperature-dependent viscosity, $a_o$ a typical interatomic spacing, $k_B$ Boltzmann's constant, and $N_0$ the number of potential nucleation sites. For homogeneous nucleation, $K_V$ in Eq. (1.29) is in the order of magnitude of $K_V \approx 10^{+39}$ $m^{-3}$ $s^{-1}$ [52] or $K_V \approx 10^{+42}$ $m^{-3}$ $s^{-1}$ [53] because each atom in the melt can act as a potential nucleation site, $N_0 = N_A/V_m$. In case of heterogeneous nucleation, only atoms at the catalyzing substrate can act as a nucleation site. Therefore $N_0$, and hence $K_V$, is drastically reduced as compared with homogeneous nucleation.

Nucleation is a stochastic process of rare and independent events. Therefore, the Poisson distribution is applied to determine $K_V$ and $C$ of Eq. (1.29) from the distribution function of the measured undercoolings. Under nonisothermal conditions (cooling rate $\dot{T} \neq 0$), the probability for one nucleation event in a sample of volume $V$ ($N_n = N_0 V$) is given by

$$\omega(1, T + \delta T) = \delta T \frac{V\, I_{ss}(T)}{|\dot{T}|} \div \exp\left[-\int_{T_m}^{T} \frac{V\, I_{ss}(T)}{\dot{T}} \mathrm{d}T\right] \qquad (1.30)$$

From Eqs. (1.26)–(1.28) the cumulative distribution function $F(T)$ is determined

$$F(T) = 1 - \exp\left[-\frac{V}{\dot{T}}\int_{T_m}^{T} K_V \cdot \exp\left(\frac{CT^2}{\Delta T^2}\right) \mathrm{d}T\right] \tag{1.31}$$

Figure 1.14 shows the distribution functions of undercoolings measured in the electromagnetic levitator (Figure 1.14 left) and the electrostatic levitator (Figure 1.14 right). Large undercoolings were achieved by levitation techniques. In case of electrostatic levitation, the undercoolings are by about 50 K larger than that in case of electromagnetic levitation. From the analysis within the Skripov model, the activation energy $\Delta G^*$ and the prefactor in the nucleation rate, $K_V$, are inferred. Both quantities are characterizing the nucleation process. In case of electromagnetic levitation, the analysis suggests heterogeneous nucleation to be dominant. The investigations by using the electrostatic levitator hint on maximum undercoolings as limited by the onset of homogeneous nucleation. Assuming homogeneous nucleation, the solid–liquid interfacial energy is estimated within classical nucleation theory, which is otherwise not accessible for experimental determination.

Equation (1.29) in combination with the results of the statistical analysis yields the product $\alpha \cdot f(\vartheta)^{1/3} = 0.61$ for Zr from the undercooling experiments in the ESL. In the literature, a great variety of dimensionless solid–liquid interfacial energies are reported from modeling work. From the present investigations, the different approaches of solid–liquid interface modeling are evaluated by comparing the modeling results with findings inferred from maximum undercooling of Zr in electrostatic levitation experiments. Since the prefactor $K_V$ is comparable in the order of magnitude to the value given by Turnbull for homogeneous nucleation, $f(\vartheta) \approx 1$ is assumed. This leads to a lower limit of the dimensionless interfacial energy $\alpha \geq 0.61$. The comparison with the modeling results shows that the negentropic model with $\alpha = 0.70$ [51] gives the best agreement with the present experiment. Density-functional yields $\alpha = 0.46$ and $\alpha = 0.48$ [54] and molecular dynamics simulations yields $\alpha = 0.29$, $\alpha = 0.32$, and $\alpha = 0.36$, respectively [55], depending on the potentials used for the simulations. All these values underestimate the solid–liquid interfacial energy inferred from the experiments. Only the negentropic model by Spaepen is in agreement with the experiments. More details are given in Ref. [56].

### 1.3.3
### Electromagnetic Levitation in Reduced Gravity

The application of electromagnetic levitation on Earth is limited by several restrictions. The strong electromagnetic fields needed to compensate the gravitational force cause strong stirring effects in the liquid and, hence, disturb mass and heat transport that influence solidification. As previously mentioned, temperature control is very difficult and needs in most cases gas convective cooling. This excludes processing under UHV conditions. In addition, the strong electromagnetic levitation fields exert a magnetic pressure on the liquid sample that leads to strong deviations from a

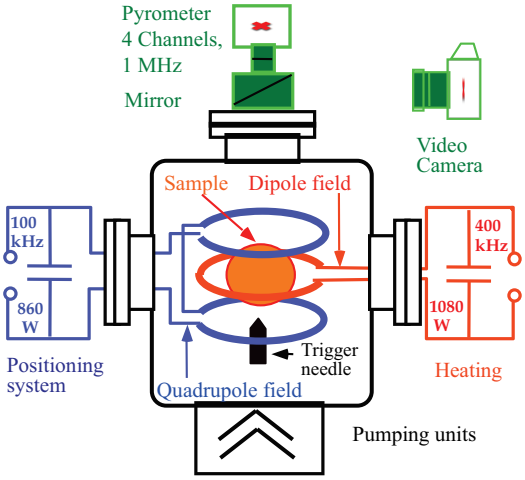


**Figure 1.15** Schematic view of the TEMPUS facility. All subsystems are shown with the exception of the radial temperature detector.

sphere-like geometry, which is needed for measurements of surface tension and mass density. These limitations are overcome if electromagnetic levitation technique is applied in reduced gravity. In the environment of space, the forces to compensate disturbing accelerations are of some orders of magnitude smaller compared with experiments on ground. A special instrument called TEMPUS has been designed to provide means of containerless processing in space [57].

A schematic view of the TEMPUS concept is shown in Figure 1.15. Positioning and heating is separated in TEMPUS by placing the sample into the superposition of a quadrupole and a dipole field of two independent coil systems. Both coil systems are powered independently by two rf generators at different radio frequencies. This two-coil concept has led to a drastic increase in the heating efficiency of levitated drops compared to usual levitation on Earth [7]. The coil system is integrated in a UHV chamber, which is evacuated by means of a turbomolecular pump to a pressure of about $10^{-8}$ mbar. The recipient can be backfilled with high purity Ar, He, and/or He-3.5%$H_2$ processing gas. Solidification of the undercooled melt can be externally triggered by touching the sample with a nucleation trigger needle, which is an integral part of the sample holder. The samples are transferred into the coil system from sample storage within ceramic cups or refractory metal cages.

TEMPUS is equipped with pyrometers and video cameras. The sample is observed from two orthogonal views. From the top, a pyrometer measures the temperature with a frequency of 1 kHz. A video camera is included in the optical path for sample observation with a maximum frame rate of 400 Hz. From the side, two different instruments can be installed, either a pyrometer specialized for measurements of the crystal growth velocity at rates up to 1 kHz (RAD), which is combined with a video camera with frame rates up to 400 Hz, or a high-resolution video camera (RMK) with

special optics. The resolution is $10^{-4}$ for an 8-mm sample as required for measurements of the thermal expansion. TEMPUS was successfully flown by NASA Spacelab missions IML2 (International Microgravity Laboratory 1994) and MSL1/MSL1R (Materials Science Laboratory 1997).

TEMPUS is especially suited to perform undercooling experiments on metals and alloys under microgravity. Different classes of experiments can be conducted. Solidification experiments by undercooling and measuring multistep recalescence profiles provide information on primary crystallization of metastable crystallographic phases. Measurements of the growth velocity as a function of undercooling are interesting with respect to the formation criteria for nonequilibrium microstructures. They also give insight into growth phenomena, where influences of convection and fluid flow play a role in, for example, dendritic/eutectic growth behavior and its influence on pattern formation in microstructure development (cf. Chapter 11).

The electromagnetic positioning of near-spherical samples in microgravity is suitable to measure the mass density of liquid metals with high accuracy. The change in diameter of a levitated sphere as a function of temperature is observed by an optical arrangement imaging the profile of the droplet [58]. Precursor experiments on Ni in terrestrial levitation experiments have demonstrated their feasibility. However, the deviation from spherical symmetry of the liquid sample due to the strong levitation fields limits the accuracy of these measurements on Earth, a problem, which was solved by experiments in space [59]. The frequency of the positioning coil current depends on the inductivity of the whole system consisting of coil and sample. The inductivity and, consequently, the frequency will change if the electrical resistivity of the sample increases with temperature. A new method has been developed to apply this principle to measure the temperature change of the electrical resistivity of molten and undercooled droplets [60]. A method based upon an AC modulation of the heating coil current has been proposed [61] and tested [62] to measure the specific heat of undercooled melts processed in a microgravity environment, using the TEMPUS instrument. A modulation of the heating coil current also excites surface oscillations of a freely suspended liquid. The oscillating drop method is used to measure the surface tension and the viscosity of levitated drops [63].

The TEMPUS facility had its maiden flight on board of NASA's Spacelab Mission of the International Microgravity Laboratory IML-2 in 1994. The technical operation of the device with all subsystems worked nominally during the entire mission of 14 days. Important scientific results have been obtained. The element Zr was melted and undercooled several times. Melting of Zr requires a temperature of more than 2125 K – this means it was the highest temperature ever achieved in the Spacelab [8]. TEMPUS was reflown on board of NASA's Spacelab Missions Materials Science Laboratory MSL-1 and MSL-1R in 1997. Altogether 17 different experiments of 10 research groups were performed. Experimental results of relevance to the present topic of metastable phases have been obtained. Studies of nucleation statistics in the microgravity environment were conducted on Zr and analyzed within nucleation theory [64]. Formation of metastable ferrite phase in Fe–Ni–Cr steel alloys were studied showing an essential influence of reduced forced convection on the life time of a primary solidified metastable phase [65]. Dendrite growth velocities on metallic

systems have been measured in space [66]. Since these Spacelab missions TEMPUS was used as multiuser facility during several parabolic flight missions and in four TEXUS sounding rocket missions very successfully.

In a common effort by DLR Space Agency and ESA, an Electro-Magnetic Levitator (EML) is currently under development for its use on board the ISS. It is under construction by ASTRIUM. Comparing with TEMPUS, some important improvements will be realized. The first one concerns the coil design. While TEMPUS used two different coils, the EML facility will make use of a new concept [67] such that only one coil system carries two different high-frequency alternating currents. The first one operates at a frequency of 135–155 kHz and serves as positioning system, whereas the second one operates at a frequency of 365–390 kHz and provides efficient heating. At maximum power, the positioning force in radial direction is about 80% and in axial direction about 120% of the force of the two-coil system of TEMPUS. The heating efficiency of EML is by a factor of 1.6 higher and the maximum heating power in the sample is about 30% higher compared with TEMPUS. The EML facility is equipped with axial temperature measurement and video observation of the sample. The temperature of the sample is measured by a one-color pyrometer in axial direction in the range between 573 K and 2373 K at an integration time of 5 ms and an accuracy of less than 0.1 K at temperatures greater than 873 K and less than 3.0 mK in the temperature range 573–673 K. The measurement rate amounts to 100 Hz. An axial digital video camera allows one to observe the sample during processing. The maximum resolution is $1280 \times 1024$ pixels and the frame rate ranges between 15 and 200 Hz depending on the pixel density. In addition to the pyrometer and video system working in axial direction, a high-speed camera is used to observe the propagation of a rapidly moving solidification front. The maximum measuring frequency is 30 kHz at a pixel density of $256 \times 256$ pixels. Also, thermal radiation monitoring from radial view is possible. Supported by the national agencies and the European Space Agency, several international researcher teams are preparing experiments using the EML on board the ISS. These experiments are divided into four different classes: (i) solidification, (ii) measurements of surface tension and viscosity, (iii) measurements of thermodynamic properties, and (iv) measurements of the mass density and thermal expansion.

## 1.4 Summary and Conclusions

It was demonstrated that levitation processing is very suitable to study solidification of undercooled melts. Undesired side effects of the levitation technique, like sample deformation and electromagnetically induced convection, can be minimized in a microgravity environment, providing benchmark data. This technique allows one to undercool and observe rapid solidification of bulk melts with a diameter of several millimeters. Thus, phase selection, dendrite growth dynamics, and grain refinement in metallic melts can be studied. Future experiments during long-term experimental campaigns on board the ISS will offer the unique possibility to test various theoretical

concepts for rapid solidification without disturbing effects by gravitational phenomena such as convection.

## Acknowledgments

The author thanks Stefan Klein for useful discussions. The presented article was produced by the European Space Agency's International Topical Team on *Solidification of Containerless Undercooled Melts* (SOL-EML) under Contract number 22971/09/NL/VJ. The author is grateful for permission by the ESA to publish this work.

## References

1 Herlach, D.M., Gillessen, F., Volkmann, T., Wollgarten, M., and Urban, K. (1992) Phase selection in undercooled quasicrystal forming Al–Mn alloy melts. *Phys. Rev. B*, **46**, 5203.

2 Rathz, T.J., Robinson, M.B., Hofmeister, W.H., and Bayuzick, R.J. (1990) The marshall space flight center drop tube facility. *Rev. Sci. Instrum.*, **61**, 3846.

3 Tournier, S., Vinet, B., Pasturel, A., Ansara, I., and Desre, P.J. (1998) Undercooling-induced metastable A15 phase in the Re–W system from drop-tube processing. *Phys. Rev. B*, **57**, 3340.

4 Kui, H.W., Greer, A.L., and Turnbull, D. (1984) Formation of bulk metallic glass by fluxing. *Appl. Phys. Lett.*, **45**, 615.

5 Herlach, D.M. (1991) Containerless undercooling and solidification of pure metals. *Annu. Rev. Mater. Sci.*, **21**, 21.

6 Rulison, A.P.J. and Rhim, W.K. (1994) A noncontact measurement technique for the specific heat and total hemispherical emissivity of undercooled refractory materials. *Rev. Sci. Instrum.*, **65**, 695.

7 Herlach, D.M., Willnecker, R., and Lohöfer, G. (1989) *Vorrichtung zum behälterlosen Schmelzen von Metallen oder Legierungen im Weltraum,* German patent DE 3639973 C2.

8 Team TEMPUS, Containerless processing in space: recent results, in *Materials and Fluids Under Low Gravity* (eds L. Ratke, H. Walter, and B. Feuerbacher 1996), Springer, Berlin, p. 233.

9 Bayuzick, R.F., Hofmeister, W.H., and Robinson, M.B. (1987) Review of drop towers and long drop tubes, in *Undercooled Alloy Phases* (eds E.W. Collings and C.C. Koch), Metallurgical Society, Warrendale, PA, p. 207.

10 Shong, D.S., Graves, J.A., Ujiie, Y., and Perepezko, J.H. (1987) Containerless processing of undercooled melts. *Mater. Res. Soc. Symp. Proc.*, **87**, 17.

11 Drehman, A.J. and Turnbull, D. (1981) Solidification behavior of undercooled $Pd_{83}Si_{17}$ and $Pd_{82}Si_{18}$ liquid droplets. *Scripta Metall. Mater.*, **15**, 543.

12 Elder, S.P. and Abbaschian, G.J. (1990) Supercooling and rapid solidification using EM levitation, in *Principles of Solidification and Materials Processing* (eds R. Trivedi, A. Sekhar, and J. Mazumdar), Oxford and IBH Publishing Co. Pvt Ltd., Delhi, p. 299.

13 Cochrane, R.F., Herlach, D.M., and Willnecker, R. (1993) Grain refinement produced by solidification into undercooled melts, in *Metastable Microstructures* (eds D. Banerjee and L.A. Jacobson), Oxford and IBH Publishing Co. Pvt Ltd., New Delhi, p. 67.

14 Gillessen, F. and Herlach, D.M. (1988) Crystal nucleation and glass-forming ability of Cu–Zr in a containerless state. *Mater. Sci. Eng. A*, **97**, 147.

15 Cochrane, R.F., Evans, P.V., and Greer, A.L. (1988) Containerless solidification of alloys in a drop tube. *Mater. Sci. Eng. A*, **98**, 99.

16 Gillessen, F. (1989) OT Keimbildungskinetik in unterkühlten, glasbildenden Metallschmelzen, Ph.D. Thesis, Ruhr-Universität Bochum, Germany.
17 Forthaus, M.,unpublished results.
18 Shechtman, D., Blech, I., Gratias, D., and Cahn, J.W. (1984) Metallic phase with long-range orientational order and no translational symmetry. *Phys. Rev. Lett.*, **53**, 1951.
19 Gillessen, F. and Herlach, D.M. (1991) Nucleation and formation of quasicrystalline phase in undercooled Al–Mn melts. *Mater. Sci. Eng. A*, **134**, 1220.
20 Avrami, M. (1939) Kinetics of phase change. *J. Chem. Phys.*, **7**, 1103.
21 Schroers, J., Holland-Moritz, D., Herlach, D.M., and Urban, K. (2000) The kinetics of growth of quasicrystalline and polytetrahedral phases from the undercooled melt. *Phys. Rev. B*, **61**, 14500.
22 Mueller, B.A., Schaefer, R.J., and Perepezko, J.H. (1987) The solidification of aluminum–maganese powders. *J. Mater. Res.*, **2**, 809.
23 Rathz, T.J., Robinson, M.B., Hofmeister, W.H., and Bayuzick, R.J. (1990) The marshall space flight center drop tube facility. *Rev. Sci. Instrum.*, **61**, 3846.
24 Vinet, B., Cortella, L., Favier, J.J., and Desre, P. (1991) Highly undercooled W and Re drops in an ultrahigh-vacuum drop tube. *Appl. Phys. Lett.*, **58**, 97.
25 Lacy, L.L., Robinson, M.B., and Rathz, T.J. (1981) Containerless undercooling and solidification in drop tubes. *J. Cryst. Growth*, **51**, 47.
26 Rony, P.R. (1964) The electromagnetic levitation of metals. Tech. Rep. UCRL-11411, Lawrence Radiation Lab., University of California, Berkeley (USA).
27 Klein, S. (2010) Nucleation in undercooled melts of pure zirconium and zirconium based alloys, Ph.D. thesis work, Ruhr-University Bochum.
28 Fromm, E. and Jehn, H. (1965) Elektromagnetische Kraftwirkung beim Levitationsschmelzen. *Zeitschrift für Metallkunde*, **56**, 599.
29 Fromm, E. and Jehn, H. (1967) Elektromagnetische Kraftwirkung beim Levitationsschmelzen. *Zeitschrift für Metallkunde*, **58**, 566.
30 Herlach, D.M., Galenko, P.K., and Holland-Moritz, D. (2007) *Metastable Solids from Undercooled Melts, Pergamon Materials Series* ELSEVIER, Oxford.
31 Sauerland, S. (1993) Messung der Oberflächenspannung an levitierten flüssigen Metalltropfen, Ph.D. Thesis, RWTH Aachen.
32 Herlach, D.M., Willnecker, R., and Gillessen, F. (1984) Containerless undercooling of Ni. Proceedings 4th European Symposium on Materials Sciences under Microgravity, **ESA SP-**222 (1984 Schloß Elmau), p. 399.
33 Karma, A. (1998) Model of grain refinement in solidification of undercooled melts. *Int. J. Non-Equilib. Pr.*, **11**, 201.
34 Schwarz, M., Karma, A., Eckler, K., and Herlach, D.M. (1994) Physical mechanism of grain refinement in solidification of undercooled melts. *Phys. Rev. Lett.*, **73**, 1380.
35 Schleip, E., Willnecker, R., Herlach, D.M., and Görler, G.P. (1988) Measurements of ultra-rapid solidification rates in greatly undercooled bulk melts by a high speed photosensing device. *Mater. Sci. Eng. A*, **98**, 39–42.
36 Schleip, E., Herlach, D.M., and Feuerbacher, B. (1990) External seeding of a metastable metallic phase. *Europhys. Lett.*, **11**, 751.
37 Cech, R.E. (1956) Undercooling of Fe-Ni droplets. *Transactions AIME*, **206**, 585.
38 Cech, R.E. and Turnbull, D. (1956) Microscopic observation of the solidification of small metal droplets. *Transactions AIME*, **206**, 124.
39 Kim, Y.-W., Lin, H.-W., and Kelly, T.F. (1988) Solidification structures in submicron spheres of iron–nickel: experimental observations. *Acta Metall. Mater.*, **36**, 2525.
40 Lin, H.-M., Kim, Y.-W., and Kelly, T.F. (1988) Solidification structures in submicron spheres of iron–nickel: analytical evaluation. *Acta Metal. Mater.*, **36**, 2537.
41 Notthoff, C., Franz, H., Hanfland, M., Herlach, D.M., Holland-Moritz, D., and

Petry, W. (2000) Energy-dispersive X-ray diffraction combined with electromagnetic levitation to study phase-selection in undercooled melts. *Rev. Sci. Instrum.*, **71**, 3791.

**42** Notthoff, C., Feuerbacher, B., Frans, H., Herlach, D.M., and Holland-Moritz, D. (2001) Direct determination of metastable phase diagram by synchrotron radiation experiments on undercooled metallic melts. *Phys. Rev. Lett.*, **86**, 1038.

**43** Earnshaw, S. (1842) On the nature of the molecular forces which regulate the constitution of the luminiferous ether. *Trans. Camb. Phil. Soc.*, **7**, 97.

**44** Rulison, A.J., Watkins, J.L., and Zambrano, B. (1997) Electrostaic containerless processing system. *Rev. Sci. Instrum.*, **68**, 2856.

**45** Meister, T. (2000) Aufbau und Regelung eines elektrostatischen Positionierers, Ph. D. thesis work, Ruhr-University Bochum.

**46** Felici, N. (1966) Forces et charges de petits objects en contact avec une électrode affectée d'un champ électrique. *Revue Générale d'Electricité*, **75**, 1160.

**47** Meister, T., Werner, H., Lohöfer, G., Herlach, D.M., and Unbehauen, H. (2003) Gain-scheduled control of an electrostatic levitator. *Engineering Practice*, **11**, 117.

**48** Skripov, V.P. (1977) *Material Science, Crystal Growth and Materials*, North Holland, Amsterdam.

**49** Christian, J.W. (1975) *The Theory of Transformations in Metals and Alloys*, Pergamon, Oxford.

**50** Turnbull, D. (1950) Formation of Crystal Nuclei in Liquid Metals. *J. Appl. Phys.*, **21**, 1022.

**51** Nelson, D.R. and Spaepen, F. (1989) Polytetrahedral order in condensed matter, in *Solid State Physics*, Academic, New York.

**52** Turnbull, D. (1969) Under What Conditions can a Glass be Formed? *Contemp. Phys.*, **10**, 473.

**53** Dantzig, J.A. and Rappaz, M. (2009) *Solidification*, EPFL Press, Switzerland.

**54** Marr, D.W. and Gast, A.P. (1993) On the solid–fluid interface of adhesive spheres. *J. Chem. Phys.*, **99**, 2024.

**55** Sun, D.Y., Asta, M., and Hoyt, J.J. (2004) Crystal–melt interfacial free energies and mobilities in fcc and bcc Fe. *Phys. Rev. B*, **69**, 174103.

**56** Klein, S., Holland-Moritz, D., and Herlach, D.M. (2009) Crystal nucleation in undercooled liquid zirconium. *Phys. Rev. B (BR)*, **80**, 212202.

**57** Piller, J., Knauf, R., Preu, P., Lohöfer, G., and Herlach, D.M. (1986) Containerless positioning and inductive heating under micro-g conditions. Proceedings 6th European Symposium on Materials Sciences under Microgravity, **ESA SP-256** (Bordeaux, 1986), p. 437.

**58** Damaschke, B., Oelgeschläger, D., Ehrich, E., Diertzsch, E., and Samwer, K. (1998) Thermal expansion measurements of liquid metallic samples measured under microgravity condition. *Rev. Sci. Instrum.*, **69**, 2110.

**59** Damaschke, B., Samwer, K., and Egry, I. (1999) Thermal expansion of glass forming metallic alloys in the undercooled state, in *Solidification 1999* (eds W.H. Hofmeister, J.R. Rogers, N.B. Singh, S.P. Marsh, and P. Vorhees) TMS, Warrendale, p. 43.

**60** Lohöfer, G. and Egry, I. (1999) Electrical resistivity measaurement in TEMPUS: results for solid, liquid, and undercooled $Co_{80}Pd_{20}$, in *Solidification 1999* (eds W.H. Hofmeister, J.R. Rogers, N.B. Singh, S.P. Marsh, and P. Vorhees), TMS, Warrendale, p. 83.

**61** Fecht, H-.J. and Johnson, W.L. (1991) A conceptual approach for noncontact calorimetry in space. *Rev. Sci. Instrum.*, **62**, 1299.

**62** Wunderlich, R.K., Lee, D.S., Johnson, W.L., and Fecht, H.-J. (1997) Non contact modulation calorimetry of metallic liquids in low Earth orbit. *Phys. Rev. B*, **55**, 26.

**63** Egry, I., Lohöfer, G., Schneider, S., Seyhan, I., and Feuerbacher, B. (1999) Thermophysical property measurements in microgravity, in *Solidification 1999* (eds W.H. Hofmeister, J.R. Rogers, N.B. Singh, S.P. Marsh, and P. Vorhees), TMS, Warrendale, p. 15.

**64** Hofmeister F W., Morton, C.M., Robinson, M.B., and Bayuzick, R.J. (1999) Experiments on nucleation in different flow regimes, in *Solidification 1999* (eds

W.H. Hofmeister, J.R. Rogers, N.B. Singh, S.P. Marsh, and P. Vorhees), TMS, Warrendale, p. 75.

65 Matson F D.M., Löser, W., and Flemings, M.C. (1999) Phase selection and rapid solidification of undercooled Fe–Cr–Ni steel alloys in microgravity, in *Solidification 1999* (eds W.H. Hofmeister, J.R. Rogers, N.B. Singh, S.P. Marsh, and P. Vorhees), TMS, Warrendale, p. 99.

66 Barth F M., Holland-Moritz, D., Herlach, D.M., Matson, D.M., and Flemings, M.C. (1999) Dendrite growth velocity measurements in undercooled Ni and Ni–C melts in space, in *Solidification 1999* (eds W.H. Hofmeister, J.R. Rogers, N.B. Singh, S.P. Marsh, and P. Vorhees), TMS, Warrendale, p. 83.

67 Lohöfer, G. (1991) *TEMPUS Space Station Vorentwicklung, SUPOS Spulenentwicklung,* German Patent 38 36239 and DLR Internal Report 333 (2001) 76.